High Temperature Reaction of MCrAlY Coating Compositions with CaO Deposits

Thomas Gheno, Gerald H Meier, Brian Gleeson

High temperature reaction of MCrAlY coating compositions with CaO deposits

Thomas Gheno, Gerald H. Meier and Brian Gleeson
Department of Mechanical Engineering and Materials Science, University of Pittsburgh, Pittsburgh PA 15261, USA
Email: thg14 at pitt.edu

This is a post-peer-review, pre-copyedit version of an article published in Oxidation of Metals. The final version is available online at:
https://doi.org/10.1007/s11085-015-9550-7

Abstract The reactivity of β–NiAl + γ-Ni-based NiCoCrAlY alloys with and without CaO deposits was studied by means of isothermal exposures in air. Reaction with CaO at 1100 °C produced multi-layer scales of Al_2O_3 and calcium aluminates, and a mixture of liquid calcium chromate and nickel–cobalt oxide particles. Calcium chromate formation was a rapid, transient process, and the transition to a steady-state of slower Al_2O_3 growth was favored by increasing the alloy β fraction. The thermally-growing Al_2O_3 reacted with the deposit to form calcium aluminates in a solid-state diffusion process, which led to an increased oxidation rate. The analysis of Al_2O_3 growth kinetics in the production-destruction regime was used to account for the increased flux of aluminum entering the multi-layer scale. The effect of temperature on the ability to kinetically sustain an Al_2O_3 scale was then evaluated on the basis of Wagner's criterion. Predicted results were consistent with the experimentally observed absence of passivation at 900 °C.

Keywords MCrAlY alloys; Multi-layer scales; Al_2O_3 growth kinetics; CaO deposits

1 Introduction

Materials used in aero, marine and land-based gas turbines need to withstand significant thermo-mechanical loads, while maintaining good environmental stability. Coatings applied to structural alloys for corrosion resistance are mainly Pt-modified nickel aluminides β–(Ni,Pt)Al, or MCrAlY (M=Ni or Co or both) based on β and the γ–Ni solid solution. Reviews of the development, processing and performance of these materials can be found in Refs. [1,2]. Thermal barrier coatings (TBCs) are used on components exposed to the highest temperatures, and possess a ceramic topcoat of yttria-stabilized zirconia (YSZ) that provides thermal insulation [3–7]. In addition to the chemically aggressive combustion atmosphere, the first stage of the high-pressure turbine is subject to deposit-induced modes of degradation, due to the ingestion of impurities from the air intake and combustion process. Calcium–magnesium alumino–silicates (CMAS) have been identified as a major source of concern for TBC systems [8–12]. When the topcoat surface reaches temperatures of 1150–1250 °C, CMAS form glassy melts which can penetrate the openings and pores needed for strain tolerance of the TBC, and, depending on their composition, dissolve the YSZ [8–12]. Little is known about the reactivity of bondcoat materials with oxide or silicate deposits at intermediate temperatures, below their melting point.

Deposits relevant to aero and land-based turbines have the common characteristic that their compositions vary widely depending on the fuel used and on the geographic location where the turbine is in service. Combustion of bituminous and anthracite coal, for example, tends to produce fly-ash rich in SiO_2 and Al_2O_3, while fly-ash from subbituminous and lignite coals contains higher levels of CaO [13]. The corrosion of Ni- and Fe-base alloys by deposits rich in CaO and $CaSO_4$ has been studied in the context of fluidized-bed combustion of coal. Results by Nagarajan et al. [14] indicated that corrosion with CaO–$CaSO_4$ deposits at 900 °C was associated with an oxidation–sulfidation process. Jung et al. [15] observed enhanced degradation in the presence of CaO during thermal cycling at 950 °C due to the formation of poorly adherent calcium aluminates, while Chiang et al. [16] reported an extremely severe type of attack due to liquid calcium chromate formation at temperatures above 1000 °C. In the case of aero turbines, recent examination of the TBC degradation on an in-service airfoil [17,18] showed that the YSZ topcoat had reacted with a CaO-rich CMAS, and was fully infiltrated by $CaSO_4$.

The work reported here is part of a larger study on the reactivity of MCrAlY coatings with fly ash relevant to integrated gasification combined cycle (IGCC) systems [19–22]. A typical bondcoat composition, Ni–20Co–16Cr–23Al–0.1Y (at. %), and a γ-rich, high Cr developmental composition, Ni–30Co–33Cr–12Al–0.1Y, were selected for testing with the following individual oxides at 1100 °C: CaO, MgO, Al_2O_3, SiO_2, Fe_2O_3. Only the relatively basic CaO and MgO had a significant impact, as their reaction with the thermally-grown Al_2O_3 produced calcium and magnesium aluminates, respectively. This paper addresses the case of reaction with CaO. The reaction mechanism and the effects of alloy composition on the extent of degradation are first discussed. Emphasis is then placed on the kinetics of the solid-state reaction between Al_2O_3 and CaO, and on the consequences this reaction has on the consumption of aluminum.

2 Materials and experimental methods

Ingots of nominal compositions (at. %) Ni–20Co–16Cr–23Al–0.1Y and Ni–30Co–33Cr–12Al–0.1Y were made by argon-arc melting, followed by drop casting into 10 mm diameter rods which were then homogenized in vacuum for 6 h at 1200 °C plus another 48 h at 1150 °C. All processing was conducted at the Materials Preparation Center of the Ames Laboratory [23]. Specimens approximately 1 mm thick were cut from the heat-treated rods, ground using SiC paper to a P1200-grit finish, then degreased with detergent and ultrasonically cleaned in ethanol before exposure.

Micrographs of the alloys after 50 h annealing in dry air at 1100 °C and air cooling are shown in Fig. 1. Both alloys exhibit a primarily β–γ microstructure at this temperature. In addition, the γ-rich Ni–30Co–33Cr–12Al–0.1Y formed 1 vol. % σ, while the β-rich Ni–20Co–16Cr-23Al–0.1Y contained a small amount ($\sim$ 0.1 vol. %) of yttrium-rich intermetallics. An even smaller amount of yttrides were present in the γ-rich alloy, reflecting the higher solubility of Y in γ. Phase compositions measured by SEM–EDS and phase fractions obtained by image analysis using the ImageJ software [24] are given in Table 1. Overall compositions calculated from these experimental results are within 0.5 at. % of the nominal compositions.

Isothermal corrosion experiments were conducted at 900 and 1100 °C in flow-

Table 1: Bulk phase compositions (SEM–EDS) and phase fractions (image analysis) of alloys Ni–20Co–16Cr–23Al–0.1Y and Ni–30Co–33Cr–12Al–0.1Y measured after 50 h heat treatment in dry air at 1100 °C. Ni–20Co–16Cr–23Al–0.1Y also contains 0.1 vol. % yttrides.

Nominal composition (at. %)	γ					β					σ				
	at. %				vol. %	at. %				vol. %	at. %				vol. %
	Ni	Co	Cr	Al		Ni	Co	Cr	Al		Ni	Co	Cr	Al	
Ni–20Co–16Cr–23Al–0.1Y	33.1	27.5	29.5	9.9	42.9	43.6	14.3	8.8	33.4	56.9					
Ni–30Co–33Cr–12Al–0.1Y	22.3	32.0	37.5	8.2	80.8	34.3	18.8	13.6	33.3	18.2	10.8	27.8	58.1	3.3	1.0

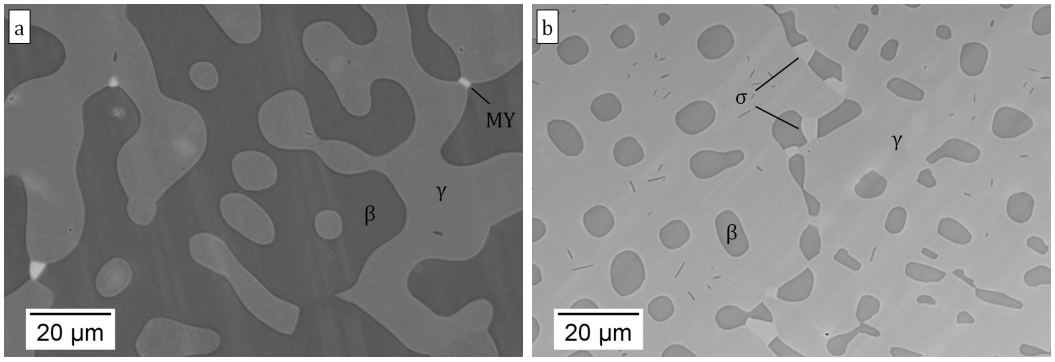

Figure 1: Micrographs of (a) Ni–20Co–16Cr–23Al–0.1Y and (b) Ni–30Co–33Cr–12Al–0.1Y after 50 h heat treatment in dry air at 1100 °C.

ing dry air, using an horizontal tube furnace. Linear gas flow rates were set to about 1 mm s^{-1} at reaction temperature, with a total pressure slightly over 1 atm. Deposits were prepared by mixing laboratory grade reagents in ethanol, and then applying the resulting slurry to one face of a given specimen using a dropper. The procedure was adjusted to produce approximately uniform 35 ± 5 mg cm^{-2} deposits after evaporation of the ethanol. In addition to time-lapse experiments, reaction kinetics were studied by thermogravimetric analysis (TGA) using a Setaram TAG thermobalance. A relatively high heating rate, 99 K/min, was chosen to reduce time spent at intermediate temperatures and hence resemble the time-lapse experiments in which the furnace was heated prior to inserting the specimens. For TGA experiments, a hole was drilled in the Ni–20Co–16Cr–23Al–0.1Y specimen, which was then dipped into the CaO slurry, and suspended in the thermobalance using Pt wire — both specimen faces were coated. As will be shown later, reaction of Ni–30Co–33Cr–12Al–0.1Y with CaO produced significant amounts of liquid. For this reason CaO was applied on one face only, and the specimen laid flat on an Al_2O_3 crucible, also suspended in the thermobalance using Pt wire. In this case the weight gain corresponding to the oxidation of the uncoated regions was subtracted from the TGA signal, on the basis of data obtained for the same alloy with no deposit. A blank test was conducted using a sample of dense Al_2O_3 coated with CaO, which confirmed that CaO did not evaporate significantly.

Mounted cross-sections were prepared using conventional metallographic techniques, and observed by SEM with a JEOL JSM 6510 instrument, equipped with an Oxford X-Max SDD EDS detector and INCA analysis software. Oxides were examined by photo-stimulated luminescence spectroscopy (PSLS), which allows γ, θ and α polymorphs of Al_2O_3 to be distinguished [25], using a 633 nm HeNe laser in a Renishaw inVia Raman microscope.

3 Results

The Ni–20Co–16Cr–23Al–0.1Y and Ni–30Co–33Cr–12Al–0.1Y alloys were reacted in dry air at 1100 °C, with and without CaO deposits, for durations ranging between 5 and 250 h. In the absence of a deposit, both alloys formed adherent Al_2O_3 scales, with no or very little oxides of Ni, Co or Cr. Scales obtained after 250 h oxidation,

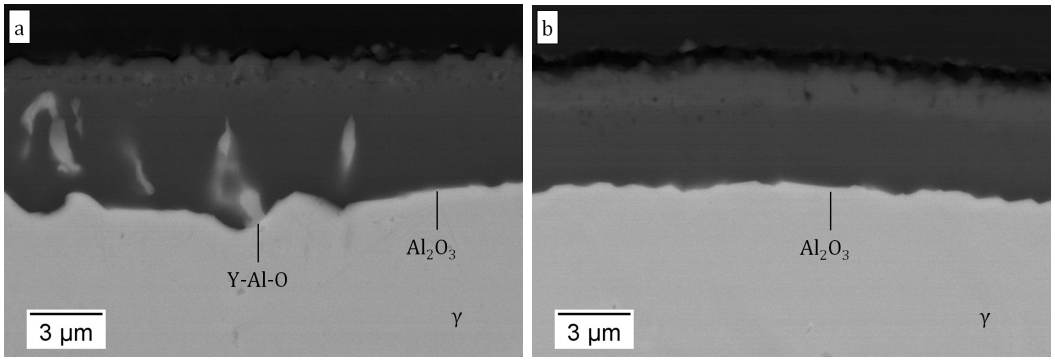

Figure 2: Alumina scales formed after 250 h oxidation of (a) Ni–20Co–16Cr–23Al–0.1Y and (b) Ni–30Co–33Cr–12Al–0.1Y in dry air at 1100 °C.

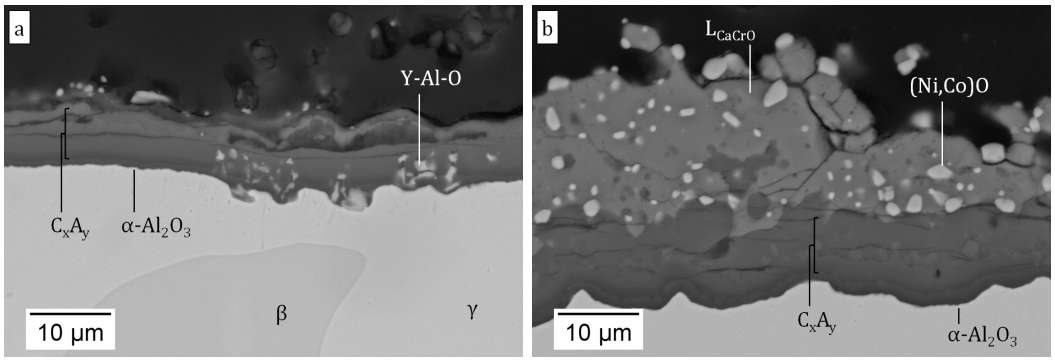

Figure 3: Reaction morphology observed after 50 h exposure of (a) Ni–20Co–16Cr–23Al–0.1Y and (b) Ni–30Co–33Cr–12Al–0.1Y in dry air with CaO at 1100 °C.

shown in Fig. 2, were thick enough for reliable chemical analysis by SEM–EDS. The outer part was thus found to contain 0.5–1 at. % Cr in Al_2O_3.

In the presence of CaO deposits, the resulting scales comprised several layers of calcium aluminates (xCaO–$y$$Al_2O_3$, denoted C_xA_y). Micrographs obtained after 50 h reaction, shown in Fig. 3, are representative of the reaction morphologies developed for all exposure durations. The layer sequence was Al-rich CA_2 nearest to the substrate, followed by equimolar CA, and occasionally the Ca-rich $C_{12}A_7$ and C_3A toward the CaO deposit. These were identified by matching compositions measured by SEM–EDS to the intermediate compounds known to exist in the CaO–Al_2O_3 system (see Fig. 4a). A thin and continuous Al-rich oxide layer, identified as α-Al_2O_3 by PSLS, was always present between the metal and the first aluminate layer. In addition, the γ-rich alloy produced a thick outer layer of calcium chromate, with (Ni,Co)O particles embedded throughout (Fig. 3b). These were occasionally found in small amounts on the β-rich alloy. It is noted that spallation of the reaction products occurred on a significant fraction of the surfaces of both alloys.

Calcium oxide is known [16] to react with the chromium contained in MCrAlY alloys to form a low-melting calcium chromate, denoted here as L_{CaCrO}, which is liquid at 1100 °C ($T_{eutectic}$ = 1061 °C, see Fig. 4b). The thickness of this layer was not uniform, which made measurements difficult. Qualitatively, the calcium chromate was found to develop rapidly on the γ-rich Ni–30Co–33Cr–12Al–0.1Y within 5

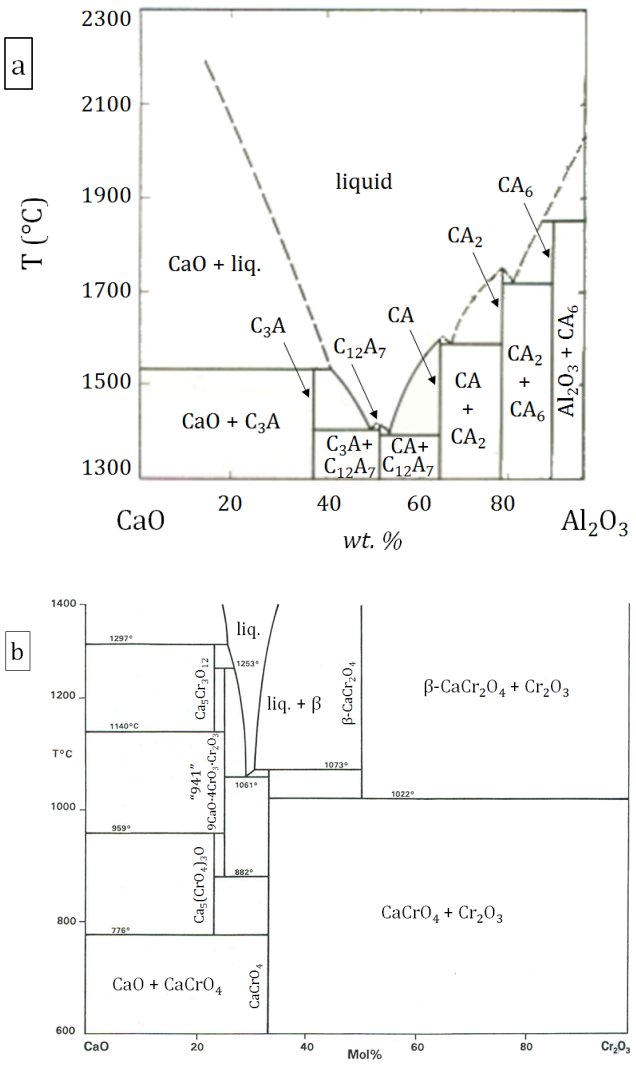

Figure 4: Pseudo-binary phase diagrams. (a) CaO–Al_2O_3 system, adapted from Ref. [26]; (b) CaO–Cr_2O_3 system, adapted from Ref. [27].

h exposure, and to not significantly thicken thereafter. The (Ni,Co)O particles did, however, grow to an appreciable extent, from an average diameter of 0.6 ± 0.2 µm after 5 h to 2.1 ± 0.7 µm after 250 h. The thickness of the β dissolution, C_xA_y and Al_2O_3 regions are plotted against the square-root of time, $t^{1/2}$, in Fig. 5, and compared with the relevant values obtained without deposit. All variables are seen to follow approximately parabolic kinetics, as expected for diffusion-controlled processes. The extent of β dissolution is much greater in Ni–30Co–33Cr–12Al–0.1Y than in Ni–20Co–16Cr–23Al–0.1Y, due to the lower starting β fraction in the former, 18 versus 57 vol. %. Alumina and C_xA_y thicknesses, however, are comparable. For both alloys, reaction with CaO yielded a thinner Al_2O_3 layer but deeper β dissolution, i.e. more extensive Al consumption, than reaction with no deposit. This will be discussed in more detail later in this paper.

The observations discussed above suggest that calcium chromate formed only during an initial transient stage. In order to test this hypothesis, Ni–20Co–16Cr–

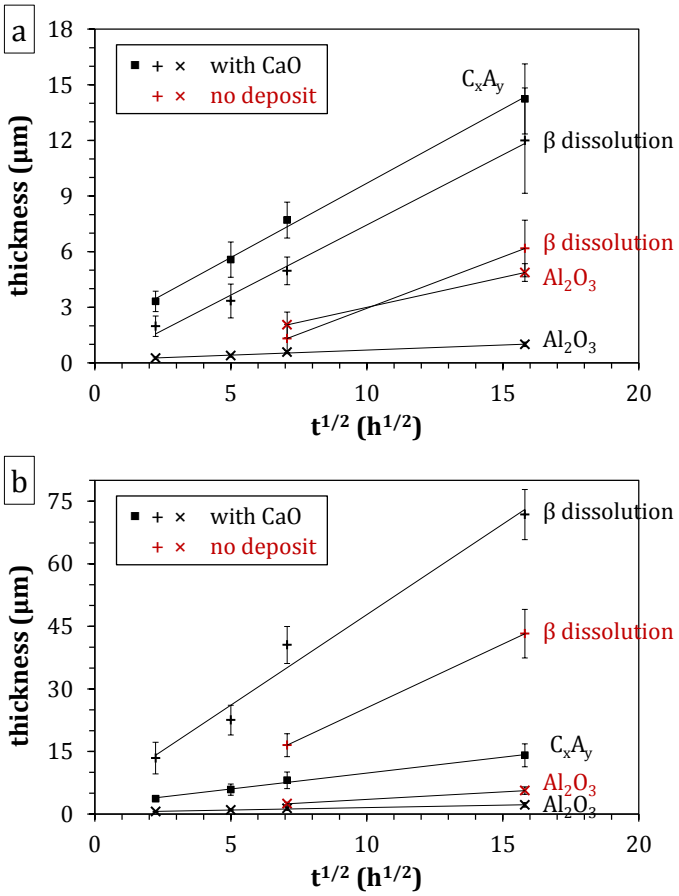

Figure 5: Thickness of reaction layers measured after exposure of (a) Ni–20Co–16Cr–23Al–0.1Y and (b) Ni–30Co–33Cr–12Al–0.1Y in dry air with and without CaO at 1100 °C.

23Al–0.1Y and Ni–30Co–33Cr–12Al–0.1Y were oxidized with no deposit in dry air for 10 h at 1100 °C, growing a continuous Al_2O_3 scale. Upon subsequent exposure to CaO for 40 h in the same conditions, the Al_2O_3 reacted to yield calcium aluminates, but no calcium chromate was formed, confirming the transient nature of the latter.

The weight gains recorded by TGA at 1100 °C, Fig. 6a, reflect the successive stages of the reaction process. Plots of $m = f(t^{1/2})$ yielded straight lines after a sufficient time was reached (not shown here). This indicates that steady-state kinetics were parabolic for both alloys, with and without CaO deposits. Reaction kinetics were further studied on the basis of the local fitting procedure described in Ref. [28]. The instantaneous parabolic constant k_p was calculated in a translating time-mass window according to

$$t = a + b\,m + c\,m^2, \tag{1}$$

where m is the weight gain per unit area, and a, b and c are constants, with $c = \frac{1}{2k_p}$. This procedure allows the reaction stages to be distinguished based on the time evolution of k_p, Fig. 6b. In the absence of CaO, Ni–20Co–16Cr–23Al–0.1Y and Ni–30Co–33Cr–12Al–0.1Y exhibited similar oxidation kinetics: a short ($\sim$ 2 h) transient stage, associated with oxides of the base metal constituents and

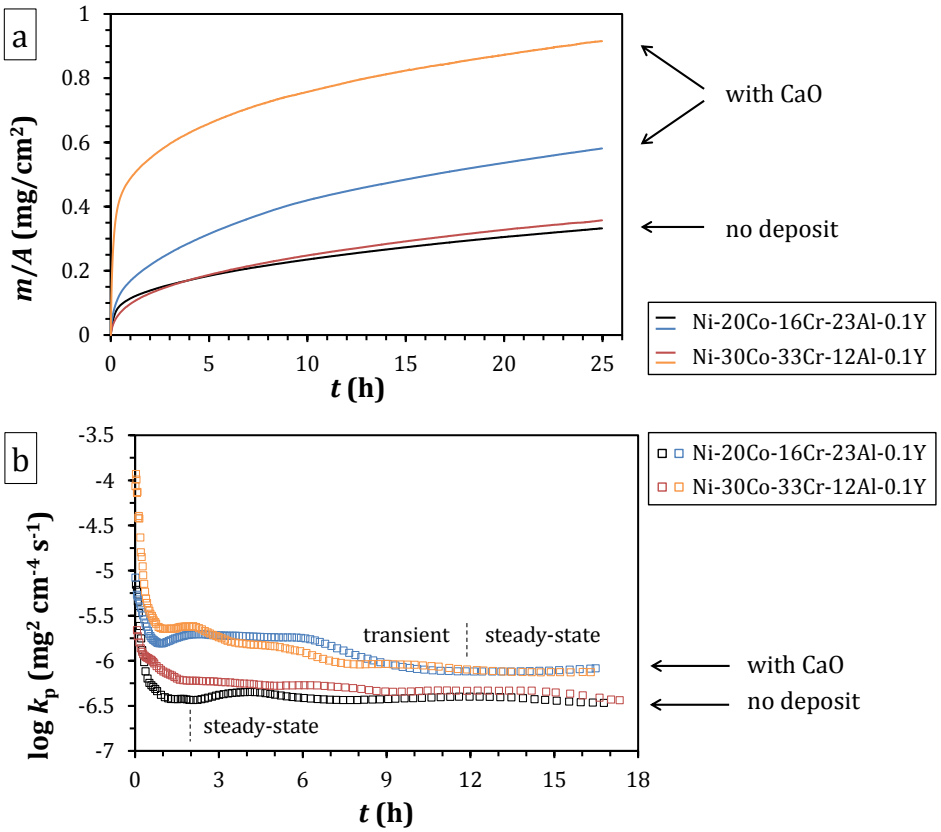

Figure 6: Reaction kinetics of Ni–20Co–16Cr–23Al–0.1Y and Ni–30Co–33Cr–12Al–0.1Y in dry air at 1100 °C, with and without CaO. (a) Weight gains recorded by TGA. (b) Local parabolic constants, determined after method in Ref. [28].

metastable alumina polymorphs, was followed by a steady-state corresponding to α-Al_2O_3 growth. Parabolic constants calculated by fitting Eq. (1) to TGA data over a 2–25 h window were found to be 3.7×10^{-7} and 4.5×10^{-7} mg^2 cm^{-4} s^{-1} for Ni–20Co–16Cr–23Al–0.1Y and Ni–30Co–33Cr–12Al–0.1Y, respectively, in good agreement with previously reported values for the growth of α-Al_2O_3 at this temperature [29–31]. In the presence of a CaO deposit, the rates of both transient and steady-state stages increased, and the transition was delayed. The effect of CaO was particularly marked in the case of Ni–30Co–33Cr–12Al–0.1Y, which exhibited a relatively large weight gain in the beginning of the reaction. Since a thick L_{CaCrO} + (Ni,Co)O layer formed on this alloy within 5 h exposure, and only small amounts were found on Ni–20Co–16Cr–3Al–0.1Y, the elevated reaction rate is attributed to L_{CaCrO} and (Ni,Co)O formation. As Fig. 6b indicates, this accelerated process was particularly short-lived (< 1 h). Until about 9 h exposure, both alloys maintained a relatively high reaction rate. The rate-limiting process associated with this period is not readily ascertained, as a continuous α-Al_2O_3 layer was identified by PSLS at the base of the scale for both alloys after 5 h reaction. Nevertheless, both alloys did passivate, and the k_p's eventually reached lower, approximately stable values.

An additional experiment was conducted with a Ni–33Co–35Cr–7Al–0.1Y alloy, which is single-phase γ at 1100 °C, and has a composition similar to that of the γ

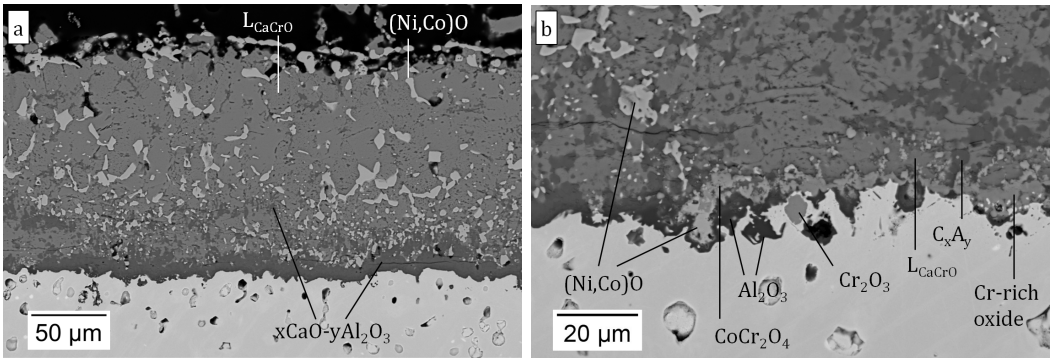

Figure 7: Reaction morphology observed after 50 h exposure of 100 % γ alloy Ni–33Co–35Cr–7Al–0.1Y in dry air with CaO at 1100 °C. (a) overview; (b) metal/oxide interface in a zone where no continuous Al_2O_3 layer is present at the base of the scale.

in Ni–30Co–33Cr–12Al–0.1Y at this temperature (see Table 1). After 50 h exposure to CaO, the 100 % γ alloy developed a reaction morphology similar to that on Ni–30Co–33Cr–12Al–0.1Y. However, the amount of L_{CaCrO} and (Ni,Co)O formed before passivation was much greater, and the $\sim$ 150 µm thick calcium chromate had also embedded C_xA_y particles (Fig. 7a). Furthermore, local regions were found on which passivation had not yet occurred, as no layer of C_xA_y or Al_2O_3 was present (Fig. 7b). In these regions, calcium chromate or aluminate was not directly in contact with the metal, but instead the reaction front consisted of oxides: (Ni,Co)O, Al_2O_3, Cr_2O_3, $CoCr_2O_4$, or Cr-rich oxide containing varying amounts of Ca, Cr or Co, with the Al_2O_3 and Cr_2O_3 sometimes present as large internal particles. These reaction products were identified based on chemical analysis by SEM–EDS.

Another γ-rich alloy, Ni–30Co–27Cr–12Al–0.1Y, was used in a series of experiments with Al_2O_3–40 wt. % CaO deposits at 900 and 1100 °C. At 1100 °C, the alloy formed an Al_2O_3 and C_xA_y layers, but no calcium chromate. This is attributed to the alloy Cr content, lower than that of the γ-rich alloys studied previously, and to the presence of Al_2O_3 in the deposit itself. The latter partially neutralized CaO by forming calcium aluminates in the deposit, which was detected by SEM–EDS after exposure. At 900 °C, a mixed calcium aluminate-chromate and a continuous Al_2O_3 sublayer formed on a small fraction of the alloy surface. Passivation was only local, however, and most regions were subject to internal oxidation and nitridation, as shown in Fig. 8. Close examination of the reaction morphology indicates the presence of Al_2O_3 in the form of both internal oxide particles and a discontinuous layer located below a Cr-rich, mixed-oxide scale. This sequence suggests that the alloy initially formed an external Al_2O_3 scale, but subsequently failed to sustain its growth, on most of its surface. Figure 8 also shows that an outer calcium chromate layer had formed, with mixed (Co,Ni)O particles embedded. Exposure to a CO_2–$20H_2O$–$1.6O_2$ gas mixture with the Al_2O_3–40 wt. % CaO deposit at 900 °C yielded a similar reaction morphology to that observed in air but with no nitrides, indicating that nitridation in air was not a cause of Al_2O_3 failure, but rather a consequence.

In the absence of a deposit, oxidation of this alloy at 1100 °C led to external Al_2O_3 scaling with very little transient oxides, while at 900 °C, the Al_2O_3 scale was surmounted by a layer of mixed Cr–Co–Ni oxide, and shallow ($\sim$ 1 µm deep)

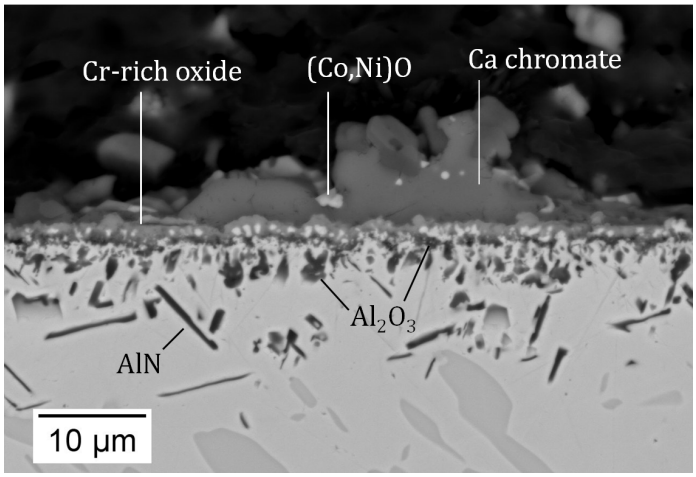

Figure 8: Reaction morphology observed after 50 h exposure of the γ-rich Ni–30Co–27Cr–12Al–0.1Y (at. %) to Al_2O_3–40 wt. % CaO in dry air at 900 °C.

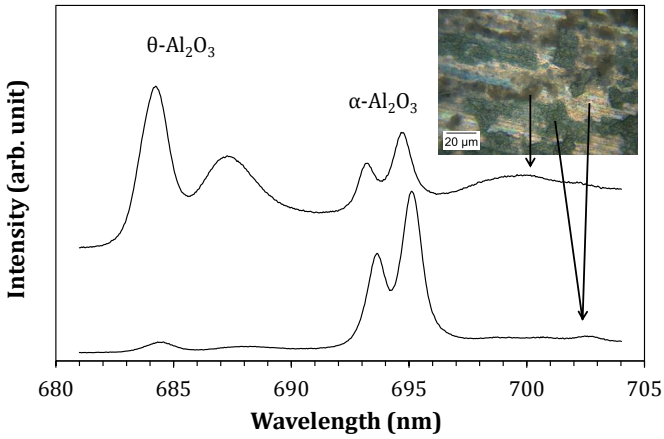

Figure 9: PSLS spectra recorded after 50 h exposure of the γ-rich Ni–30Co–27Cr–12Al–0.1Y in dry air at 900 °C, with no deposit, showing regions of α and θ-Al_2O_3. Since θ-Al_2O_3 luminescence is 10–12 times weaker than that of α-Al_2O_3 [25], the top spectrum denotes regions primarily consisting of θ-Al_2O_3.

Al_2O_3 intrusions were locally seen to grow into the alloy. Furthermore, the $\theta \rightarrow \alpha$ transformation was not complete after 50 h at 900 °C. Surface PSLS characterization showed that while most of the surface consisted of α-Al_2O_3, a significant fraction was still predominantly θ (Fig. 9).

4 Discussion

4.1 Influence of alloy composition

The case of pure CaO deposits at 1100 °C is considered first. As noted in the introduction, Chiang et al. [16] studied the reaction of nominally Al_2O_3-forming NiCrAl and CoCrAl alloys with CaO, and found that the formation of liquid calcium chromate led to very rapid alloy destruction. In the present study, the extent of metal

loss due to L_{CaCrO} and (Ni,Co)O was seen to vary quite significantly with alloy composition and, in turn, alloy microstructure. The β-rich Ni–20Co–16Cr–23Al–0.1Y rapidly established continuous Al_2O_3 and C_xA_y layers, which prevented the oxidation of Cr, Ni or Co; whereas, the 100 % γ Ni–33Co–35Cr–7Al–0.1Y sustained extensive degradation before it could passivate, and the γ-rich Ni–30Co–33Cr–12Al–0.1Y had an intermediate behavior.

Aluminum and chromium strongly partition to the β and γ phases, respectively, as seen in Table 1. Thus γ will favor L_{CaCrO} formation, while β will tend to form Al_2O_3 and C_xA_y. As suggested by Chiang et al. [16], calcium chromate is formed by reaction of CaO with transient chromium oxide. A remarkable finding is that, as mentioned in Section 3, the extent of transient Cr oxidation on the alloys studied here in the absence of a CaO deposit was very small. Thus, the reaction of CaO with chromium must be particularly rapid, which is confirmed by the TGA measurements for Ni–30Co–33Cr–12Al–0.1Y (Fig. 6). The fact that the (Ni,Co)O particles embedded in the chromate grew significantly with reaction time indicates that they did not precipitate on cooling, but instead developed at temperature. This is due to the fact that L_{CaCrO} dissolves very little ($<$ 1 at. %) nickel or cobalt oxide: as the reaction front advances into the γ-phase, Ni and Co are rejected from the liquid and precipitate as oxide particles. Similarly, the solubility of Al_2O_3 in the chromate was measured by SEM–EDS to be quite low (1–2 at. %), as also reported by Kaiser et al. [27]. This led to an Al:Cr elemental ratio of about 1:5, similar to that in the original γ phase in Ni–30Co–33Cr–12Al–0.1Y and Ni–33Co–35Cr–7Al–0.1Y. The conservation of this Al:Cr ratio indicates that the γ phase was consumed in situ by the rapidly advancing reaction front. However, some change in the boundary conditions, such as a decelerating reaction front and associated accumulation of Al in the alloy at the metal/oxide interface, must occur to allow for the eventual establishment of an Al_2O_3 layer. The Cr-rich oxides observed at the reaction front in the non-passivated zones of the 100 % γ alloy (Fig. 7) likely represent an intermediate stage between rapid liquid formation and the establishment of an Al_2O_3 layer.

Exactly how the alloy passivates remains unclear at this stage. Nevertheless, the implications of this reaction process are readily understood, in terms of alloy resistance to the severe degradation associated with liquid calcium chromate: metal loss should be minimized with a lower chromium content or a higher fraction of β. In particular, considerable resistance can be obtained by having a β fraction sufficiently high for the β phase to be continuous, as opposed to forming a dispersion in a γ matrix, as schematically represented in Fig. 10. The β-rich Ni–20Co–16Cr–23Al–0.1Y did form a very small amount of L_{CaCrO} and (Ni,Co)O (Fig. 3a); the large β fraction (57 %) simply allowed the progression of the liquid phase to be undercut by an Al_2O_3 layer sooner than in the γ-rich alloys.

4.2 Kinetics of Al_2O_3 growth at 1100 °C

The stage of rapid alloy consumption due to liquid chromate formation at 1100 °C was followed by a steady-state of slower reaction, which corresponded to the establishment of an inner continuous Al_2O_3 layer. However, this thermally growing Al_2O_3 reacted with the calcium and oxygen contained in L_{CaCrO}, or directly with the CaO deposit, to form C_xA_y. Much like evaporation of Cr_2O_3 scales in wet atmospheres, consumption of the protective oxide has consequences on the reaction kinetics, which

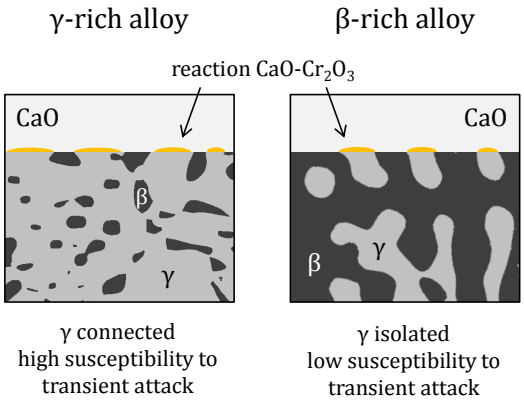

Figure 10: Schematics showing how the susceptibility for transient attack by CaO is determined by the distribution of the Cr-rich γ phase in the alloy.

are considered in the following. Quite different from evaporation, destruction of the oxide in the present case occurred via a solid-state, diffusion-controlled process.

The case of Ni–20Co–16Cr–23Al–0.1Y, where very little L_{CaCrO} formed and the outermost C_xA_y layer was in contact with the CaO deposit, is considered first. Figure 11 shows a schematic of the reaction process. Calcium aluminate growth is known to be controlled by Ca^{2+} diffusion in the solid state [32–35]; its formation is therefore described to occur at the Al_2O_3/C_xA_y interface by the reaction

$$xCa^{2+} + xO^{2-} + yAl_2O_3 = C_xA_y. \tag{2}$$

The oxygen and calcium necessary for this reaction are provided by the decomposition of CaO at the CaO/C_xA_y interface:

$$CaO = Ca^{2+} + O^{2-}. \tag{3}$$

Two processes contribute to net Al_2O_3 growth: (i) its destruction to form C_xA_y according to Eq. (2) at the Al_2O_3/C_xA_y interface, and (ii) its production by oxidation of aluminum contained in the metal substrate,

$$2Al^{3+} + 3O^{2-} = Al_2O_3. \tag{4}$$

For the sake of simplicity, Al_2O_3 production is described to occur at the metal/oxide interface, with O^{2-} assumed to diffuse faster than Al^{3+}. The choice of a mixed or predominantly outward growth mechanism would not change the resulting kinetics. As illustrated in Fig. 11, the oxygen necessary for Al_2O_3 growth is supplied by solid-state diffusion through C_xA_y. This oxygen ultimately originates from the gas atmosphere. It is further assumed that the oxygen provided by decomposition of CaO is entirely consumed to form C_xA_y. This prevents the accumulation of calcium or oxygen in C_xA_y, and is realistic insofar as all known calcium aluminates are intermediate xCaO–$y$$Al_2O_3$ compounds (Fig. 4a), in which the degree of oxidation of Ca and Al is not different from that in CaO and Al_2O_3, respectively. In the case of the γ-rich Ni–30Co–33Cr–12Al–0.1Y alloy, the C_xA_y layers are surmounted by liquid calcium chromate; it is assumed that the latter can rapidly provide the oxygen and

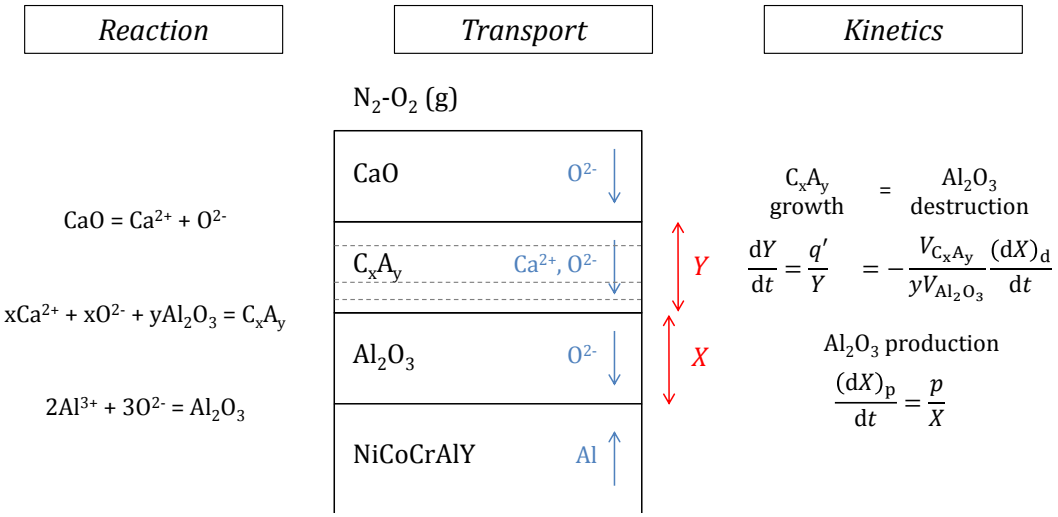

Figure 11: Schematic representation of the reactions and transport processes associated with the formation of calcium aluminate from CaO and thermally grown Al_2O_3. Variables are defined in text.

calcium required for C_xA_y and Al_2O_3 growth, and that this step is therefore not rate-limiting.

Several investigators have studied the growth kinetics of oxide scales that consist of multiple layers growing by diffusion of the same cation, taking into account the partitioning of the cation flux between the successive layers [36–41]. The present situation is slightly different in that it involves two types of cations, but it is equivalent if one considers the diffusion of oxygen instead. Provided that the degree of oxidation of aluminum and calcium does not change upon forming any of the aluminates from CaO and Al_2O_3, the present situation is a particular, simple case of the general formalism introduced by Yurek et al. [37] for two-layer structures. That treatment provided a relationship between the thickening constant measured for each layer in the multi-layer scale and the "intrinsic" constants that would be observed if a single-layer of each individual oxide had formed.

Published studies of calcium aluminate growth mostly concern powders, and the reported rate constants tend to vary significantly depending on the starting materials and the method used to assess the results. In the absence of consistent data in the literature, the present analysis will rely on experimental data obtained here. The following considers the relationship between the constants measured for Al_2O_3 and C_xA_y in the multi-layer structure and the constant for individual Al_2O_3 growth, measured in the absence of a deposit. Since the stoichiometry and relative thicknesses of the aluminates do not affect the flux of oxygen used for the oxidation reaction, the aluminate layers are gathered into a single layer of average stoichiometry C_xA_y. Its thickening kinetics are described in accordance with the parabolic rate law,

$$\frac{\mathrm{d}Y}{\mathrm{d}t} = \frac{q'}{Y}, \tag{5}$$

where Y is the thickness of C_xA_y in the Al_2O_3–C_xA_y scale, and q' is the associated

parabolic constant. Since $Y(t=0)=0$, Eq. (5) yields

$$Y^2 = 2q't. \tag{6}$$

Considering the mass balance underlying Eq. (2), the destruction of Al_2O_3 is written

$$\frac{(\mathrm{d}X)_\mathrm{d}}{\mathrm{d}t} = -\frac{yV_{Al_2O_3}}{V_{C_xA_y}}\frac{\mathrm{d}Y}{\mathrm{d}t}, \tag{7}$$

where V_i is the molar volume of phase i. Using the TGA data of Fig. 6, it can be shown that in the steady-state regime established in the absence of a deposit, Al_2O_3 grows according to parabolic kinetics. Previous findings discussed in Ref. [42] show that the rate-limiting step for Al_2O_3-scale thickening is grain-boundary diffusion of O^{2-} and Al^{3+}. This still holds when there is concurrent C_xA_y formation, so long as the alloy can provide sufficient Al to sustain Al_2O_3 growth. Inasmuch as the constitution and predominant structure of Al_2O_3 grain boundaries remain unchanged, the instantaneous growth rate in a situation of production-destruction is inversely proportional to the oxide thickness, with the same constant as in the absence of a deposit. Thus the production term is written

$$\frac{(\mathrm{d}X)_\mathrm{p}}{\mathrm{d}t} = \frac{p}{X}, \tag{8}$$

where X is the thickness of Al_2O_3 in the Al_2O_3–C_xA_y scale and p is the parabolic constant for exclusive oxidation.

The net Al_2O_3 growth is obtained by adding the two contributions, i.e., Eqs. (7) and (8):

$$\frac{\mathrm{d}X}{\mathrm{d}t} = \frac{(\mathrm{d}X)_\mathrm{p}}{\mathrm{d}t} + \frac{(\mathrm{d}X)_\mathrm{d}}{\mathrm{d}t} = \frac{p}{X} - \frac{yV_{Al_2O_3}}{V_{C_xA_y}}\frac{\mathrm{d}Y}{\mathrm{d}t} \tag{9}$$

or, using Eqs. (5) and (6),

$$\frac{\mathrm{d}X}{\mathrm{d}t} = \frac{p}{X} - \alpha\frac{q'}{\sqrt{2q't}}, \tag{10}$$

where $\alpha = \dfrac{yV_{Al_2O_3}}{V_{C_xA_y}}$. This equation is solved to yield

$$\begin{cases} X^2 = 2p't \\ p' = \dfrac{1}{2}\left[2p + \alpha^2 q' - \alpha\sqrt{q'\left(4p + \alpha^2 q'\right)}\right]. \end{cases} \tag{11}$$

The form of Eq. (10) allows for another solution $p'' = \frac{1}{2}\left[2p + \alpha^2 q' + \alpha\sqrt{q'\left(4p + \alpha^2 q'\right)}\right]$, with $p' < p < p''$. Since Al_2O_3 is being consumed by the reaction with the aluminate, p' is the appropriate solution. Noting that the valence of aluminum is the same in Al_2O_3 and C_xA_y, the same expression for p' can be obtained from the general equations given by Yurek et al. [37]. Based on that treatment, the relationships between the constants measured in the Al_2O_3–C_xA_y scale and the constants for individual Al_2O_3 and C_xA_y growth are

$$p' = \frac{p}{1 + \alpha\frac{Y}{X}} \tag{12}$$

$$q' = \frac{q}{1 + \frac{1}{\alpha}\frac{X}{Y}} \tag{13}$$

Table 2: Parabolic constants (10^{-14} cm^2 s^{-1}) for Al_2O_3 and C_xA_y growth in Al_2O_3–C_xA_y scales, and for exclusive Al_2O_3 growth, obtained from various methods (see text for details).

		Ni–20Co–16Cr–23Al–0.1Y	Ni–30Co–33Cr–12Al–0.1Y
Al_2O_3 thickness	p'	0.41	1.9
TGA (no deposit)	p	11	13
C_xA_y thickness	q'	83	80
Equation (11)	p'	2.7	3.7
TGA (with deposit)	r'	25	24
Equation (21)	p'	4.5	6.9

with the ratio of layer thicknesses in the multi-layer structure given by

$$\frac{Y}{X} = \alpha \frac{q}{p}. \tag{14}$$

The analysis is now applied to the reactions of Ni–20Co–16Cr–23Al–0.1Y and Ni–30Co–33Cr–12Al–0.1Y. For each alloy, the intrinsic oxidation rate p is arrived at by fitting the TGA data measured with no CaO (Fig. 6), while q' is determined from C_xA_y thickness measurements (Fig. 5). The ratio $\alpha = yV_{Al_2O_3}/V_{C_xA_y}$ is calculated as the average of values obtained for CA and CA_2, which were found by SEM–EDS to constitute most of the C_xA_y. Values of p' calculated with Eq. (11) are shown in Table 2, together with constants obtained from direct measurement of Al_2O_3 thickness in Al_2O_3–C_xA_y scales (Fig. 5). The latter are seen to be within an order of magnitude but significantly smaller than those obtained indirectly via Eq. (11), especially for the β-rich alloy. This will be discussed subsequently.

After evaluating reaction kinetics based on direct thickness measurements, p' is now calculated using TGA data (Fig. 6), which also reflect the rate at which the Al_2O_3 layer thickens. According to the description adopted here and represented in Fig. 11, the weight gain per unit of surface area recorded during reaction with CaO corresponds to the oxygen uptake necessary for Al_2O_3 production:

$$\frac{\mathrm{d}m}{\mathrm{d}t} = \frac{\mathrm{d}m_\mathrm{O}}{\mathrm{d}t} = \frac{(\mathrm{d}m_\mathrm{O})_\mathrm{p}}{\mathrm{d}t}. \tag{15}$$

No net weight gain arises from C_xA_y growth, as the calcium and oxygen forming the x CaO units come from the CaO deposit, and the aluminum and oxygen forming the y Al_2O_3 units come from the existing Al_2O_3. The net oxygen uptake is related to the quantity of Al_2O_3 that is produced through the mass balance underlying Eq. (4):

$$\frac{1}{M_\mathrm{O}}(\mathrm{d}m_\mathrm{O})_\mathrm{p} = (\mathrm{d}n_\mathrm{O})_\mathrm{p} = 3(\mathrm{d}n_{Al_2O_3})_\mathrm{p}, \tag{16}$$

where M_O is the atomic weight of oxygen. Combining Eqs. (15) and (16), and converting the quantity of Al_2O_3 into an equivalent thickness, one obtains

$$\frac{\mathrm{d}m}{\mathrm{d}t} = \frac{3M_\mathrm{O}}{V_{Al_2O_3}} \frac{(\mathrm{d}X)_\mathrm{p}}{\mathrm{d}t}. \tag{17}$$

Using the TGA data of Fig. 6, one can show that at steady-state, weight gains of both Ni–20Co–16Cr–23Al–0.1Y and Ni–30Co–33Cr–12Al–0.1Y in the presence of

CaO obey a parabolic law

$$m^2 = 2s't, \tag{18}$$

where s' is the gravimetric constant. It follows from Eq. (17) that Al_2O_3 production also obeys parabolic kinetics, which is written

$$\frac{(\mathrm{d}X)_\mathrm{p}}{\mathrm{d}t} = \frac{r'}{\sqrt{2r't}}, \tag{19}$$

where $r' = s' \left(V_{Al_2O_3}/3M_O\right)^2$ is the parabolic constant related to the rate at which Al_2O_3 thickens by oxidation of the alloy in the Al_2O_3–C_xA_y structure. This production rate is inversely proportional to the layer thickness, Eq. (8), which yields

$$\frac{p}{X} = \frac{r'}{\sqrt{2r't}}. \tag{20}$$

Considering that $X(t=0) = 0$, Eq. (20) is solved to provide

$$\begin{cases} X^2 = 2p't \\ p' = \dfrac{p^2}{r'}. \end{cases} \tag{21}$$

Thus p' can be calculated from r' and p, which are obtained by fitting TGA data recorded with and without CaO deposit, respectively. The results are seen in Table 2 to be in reasonable agreement with the values obtained with Eq. (11), although slightly higher.

Two observations should be made from the p' values presented in Table 2. First, for a given alloy, a significant discrepancy exists between the values obtained with the three methods used. This is particularly the case for the β-rich alloy, where the value corresponding to direct thickness measurements is much lower than the calculated values. The difference is beyond possible experimental errors, and must instead reflect the incomplete satisfaction of the limiting assumptions made here. First, analysis by SEM–EDS showed small amounts (1–2 at. %) of chromium in the C_xA_y, and of aluminum in the L_{CaCrO}. This slightly affects the mass balance underlying Eq. (11) and the interpretation of the TGA data, via Eq. (16). Furthermore, some aspects of the complexities associated with Al_2O_3 growth were not accounted for in the present analysis. For instance, one aspect is related to the choice of boundary conditions: the oxygen activity at the Al_2O_3 surface was assumed to be the same whether calcium aluminates form or not, although some p_{O_2} gradient probably exists across the layers in the Al_2O_3–C_xA_y scale. This arguably does not affect p' significantly, inasmuch as Al_2O_3 predominantly exhibits n-type behavior, and its growth rate is little affected by the external p_{O_2} [42]. Further, oxidation both with and without CaO involves a transient stage, as shown by the TGA data in Fig. 6, which possibly comprises the formation of metastable Al_2O_3 polymorphs, base-metal oxides or L_{CaCrO} prior to the establishment of α-Al_2O_3 and C_xA_y layers. One can show that the extent of these processes does not directly affect the thickening rate achieved during steady-state. (Specifically, using equations of the form $(x - x_i)^2 = 2k\,(t - t_i)$ or $x^2 - x_i^2 = 2k\,(t - t_i)$ to describe Al_2O_3 or C_xA_y growth does not change the expression giving p' in Eq. (11) for sufficiently long reaction times.) However, in accordance with the analysis of Brumm and Grabke [31], aspects of transient oxidation such as the time needed for the $\theta \rightarrow \alpha$ transformation

do have an influence on the microstructure of Al_2O_3, in particular its grain size, and therefore affect growth rates observed on the longer term. In this respect, because of the p-type nature of θ-Al_2O_3 [43–45], a reduced p_{O_2} at the oxide surface in the presence of C_xA_y could have an indirect effect on the α-Al_2O_3 eventually established, by slowing the growth of the metastable polymorph. Due to its high reactivity, the presence of CaO certainly had an impact on the transient stage of the reaction, as evident in Fig. 6, although potential effects on Al_2O_3 microstructure were beyond the scope of this investigation.

A second observation arising from the data gathered in Table 2 is that a significant difference exists between the p' values obtained for the two alloys, which is not accounted for in the present analysis. This is most evident when considering p' from direct Al_2O_3 thickness measurements. Similarly, the C_xA_y-to-Al_2O_3 thickness ratio, while approximately constant with time for each alloy as expected for diffusion-controlled growth processes, was found to be quite different for the two alloys: 12.8 ± 0.8 for Ni–20Co–16Cr–23Al–0.1Y, versus 6.2 ± 0.2 for Ni–30Co–33Cr–12Al–0.1Y. This could possibly be due to a difference in the constitution of the C_xA_y scale, as varying relative thicknesses would affect the average scale stoichiometry. This could not be assessed with sufficient accuracy because of the non-uniform, locally rumpled morphology of the reaction product. Another potential effect is related to the presence of liquid calcium chromate. In the case of the γ-rich alloy, the calcium and oxygen required for C_xA_y and Al_2O_3 growth must be provided by the L_{CaCrO} which forms a thick and continuous layer. If ionic transport in the liquid is not sufficiently rapid, it could limit the rate of C_xA_y growth, and allow a relatively thicker Al_2O_3 to persist. Furthermore, a slow transport would also involve a local chromium enrichment in the liquid, and, since the latter occupies a small composition range at 1100 °C (Fig. 4b), this could result in the precipitation of $CaCr_2O_4$. The phase transformation would involve a partial reduction of chromium (the liquid contains a mixture of Cr III and Cr VI, while $CaCr_2O_4$ contains only Cr III), which would affect oxygen both in the mass balance underlying Eq. (11) and in the interpretation of the TGA data, via Eq. (15). Again the constitution of the L_{CaCrO} could not be characterized with the degree of accuracy required because of experimental limitations.

Overall, the present results indicate that beyond a reduction in thickness, the growth mechanism of Al_2O_3 is affected by the reaction with CaO. The details of the associated processes, as well as the role played by alloy composition, are outside the scope of the present paper and deserve further investigation. Yet, the present analysis is useful in that it provides a semi-quantitative evaluation of the effect of CaO on the rate of Al consumption. In essence, as Al_2O_3 reacts to form C_xA_y, its thickness is reduced, and so is its ability to act as a diffusion barrier: the instantaneous oxidation rate p/X increases. This rate is expressed as $(\mathrm{d}X)_\mathrm{p}/\,\mathrm{d}t = p/\sqrt{2p't}$, and since $p' < p$, it is indeed larger than its CaO-free counterpart, $p/\sqrt{2pt}$. Another metric that can be used to characterize Al consumption is the rate of β dissolution. Due to the larger oxidation rate, β is dissolved at a greater rate in the presence of CaO, as seen in Fig. 5.

4.3 Effect of temperature on Al consumption in the presence of CaO

We now consider the effect of the reaction with CaO on the ability of a given alloy to maintain an Al_2O_3 layer, using Wagner's [46] criterion for sustained external scaling. Briefly, this is based on the principle that external Al_2O_3 growth can be maintained if the outward Al flux in the metal at the interface with the oxide matches the flux required for the oxide to grow. A maximum flux is obtained in the alloy when the interfacial Al content is set to zero, which in turn defines a minimum bulk concentration, N^*_{Al}. Since the flux of Al consumed by scale growth is related to the instantaneous oxide production rate, the above analysis suggests that taking into account the reaction with CaO will amount to replacing the oxidation constant p by the ratio p^2/p' in calculating N^*_{Al}.

Under the assumptions of parabolic oxidation kinetics and of a constant Al diffusion coefficient in the alloy (D_{Al}) in the composition range of interest, N^*_{Al} is given by [46]

$$N^*_{Al} = F\left(\sqrt{\frac{1}{2}\frac{k_c}{D_{Al}}}\right) \tag{22}$$

where F is the auxiliary function defined by $F(u) = \sqrt{\pi}u(1 - \operatorname{erf} u)\exp(u^2)$ and k_c the parabolic constant for metal recession, defined by $d^2 = 2k_c t$ with d the depth of the metal/oxide interface relative to the original alloy surface. In a situation of individual Al_2O_3 growth, the mass balance on the aluminum contained in the oxide scale is written

$$\frac{2X}{V_{Al_2O_3}} = \frac{d}{V_a} \tag{23}$$

with V_a the molar volume of the alloy, which yields a simple relationship between k_c and p

$$k_c = \left(\frac{2V_a}{V_{Al_2O_3}}\right)^2 p. \tag{24}$$

This is now introduced in Eq. (22) to give

$$N^*_{Al} = F\left(\frac{2V_a}{V_{Al_2O_3}}\sqrt{\frac{p}{2D_{Al}}}\right). \tag{25}$$

When Al_2O_3 reacts with CaO to form calcium aluminates, the mass balance of Eq. (23) becomes

$$\frac{2X}{V_{Al_2O_3}} + \frac{2yY}{V_{C_xA_y}} = \frac{d}{V_a}. \tag{26}$$

Using Eqs. (6) and (11), Y can be given as

$$Y = \frac{V_{C_xA_y}}{yV_{Al_2O_3}}\left(\sqrt{2\frac{p}{p'}t} - X\right) \tag{27}$$

and the relationship giving k_c from measurable constants becomes

$$k_c = \left(\frac{2V_a}{V_{Al_2O_3}}\right)^2 \frac{p^2}{p'} \tag{28}$$

which finally yields

$$N^*_{\mathrm{Al}} = F\left(\frac{2V_{\mathrm{a}}}{V_{\mathrm{Al_2O_3}}}\sqrt{\frac{p^2/p'}{2D_{\mathrm{Al}}}}\right). \tag{29}$$

A comparison between Eqs. (24) and (28) confirms that changing from an individual Al_2O_3 scale to a multi-layer Al_2O_3–C_xA_y scale amounts to replacing p by p^2/p' when considering the flux of Al incorporated in the reaction product.

This analysis is now used to study the effect of a varying temperature on the reaction of Ni–30Co–27Cr–12Al–0.1Y with Al_2O_3–CaO deposits. No measured value of p or p' is available for this alloy; instead, N^*_{Al} is evaluated as follows. The constant p is taken from data by Brumm and Grabke [31] for α and θ-Al_2O_3 growth on NiAl–Cr alloys, using activation energies of 350 and 231 kJ/mol, respectively. In the absence of direct data, q is first calculated at 1100 °C from Eqs. (13) and (14) using q' measured here for Ni–30Co–33Cr–12Al–0.1Y (Table 2) and p for α-Al_2O_3 in Ref. [31]. Activation energies reported in the literature for the growth of calcium aluminates vary widely [33], with most values in the 150–250 kJ/mol range [35]; the median 200 kJ/mol is used here, in good agreement with results reported in Refs. [32, 34]. Values of q at varying temperatures are then calculated from q at 1100 °C, based on the Arrhenius equation. Constants p' and q' are then obtained for each of α and θ-Al_2O_3 using Eqs. (12–14) and the constants for individual Al_2O_3 (p) and C_xA_y (q) growth. Interdiffusion in a 5-component, 2-phase alloy system is complex. Since β is quite rapidly depleted from the subsurface of the γ-rich alloys, only diffusion in γ is considered. Nesbitt and Heckel [47] published experimental interdiffusion data for the ternary Ni–Cr–Al system, including a regression equation allowing interdiffusion coefficients to be calculated as a function of alloy composition. Chromium concentration gradients were seen to have little effect on Al diffusion, such that the main term $\tilde{D}^{\mathrm{Ni}}_{\mathrm{Al,Al}}$ was prevalent. At 1100 °C, replacing Co by Ni and ignoring Y, one calculates $\tilde{D}^{\mathrm{Ni}}_{\mathrm{Al,Al}} = 3.4\times10^{-10}$ cm^2 s^{-1} for the nominal composition (27Cr, 12Al), and $\tilde{D}^{\mathrm{Ni}}_{\mathrm{Al,Al}} = 1.1\times10^{-10}$ cm^2 s^{-1} for an alloy fully depleted of its Al. Equation (29) is based on a constant diffusion coefficient; the average value $\tilde{D}^{\mathrm{Ni}}_{\mathrm{Al,Al}} = 2\times10^{-10}$ cm^2 s^{-1} is chosen as an approximation. This value is consistent with other experimental and calculated values for dilute NiCrAl alloys at 1100 °C gathered in Ref. [48]. The activation energy for $\tilde{D}^{\mathrm{Ni}}_{\mathrm{Al,Al}}$, 288 kJ/mol, is taken from Ref. [47].

Minimum Al concentrations calculated using Eq. (29) are plotted as a function of temperature in Fig. 12 for both α and θ-Al_2O_3 growth, with and without CaO reaction. All predicted N^*_{Al} values are below the alloy nominal Al content (12 at. %). Considering α-Al_2O_3 at 1100 °C, the reaction with CaO leads to a relatively small increase of N^*_{Al}, from 1.2 at. % with no deposit to 2.8 at. % with CaO. This is consistent with the observed ability of Ni–30Co–27Cr–12Al–0.1Y to maintain an external Al_2O_3 layer at this temperature. For α-Al_2O_3 reaction with CaO, the 900 °C value of N^*_{Al}, 4.9 at. %, is higher than the 1100 °C value, but still relatively low. This indicates that the decrease in the alloy diffusion rate is partly compensated by the slowing of diffusion in Al_2O_3 and C_xA_y. However, PSLS measurements (Fig. 9) showed that θ-Al_2O_3 was still present in significant amounts after 50 h at 900 °C, which suggests that the metastable polymorph controlled the oxidation rate for an extended period at this temperature. Indeed, several investigators [30, 31,

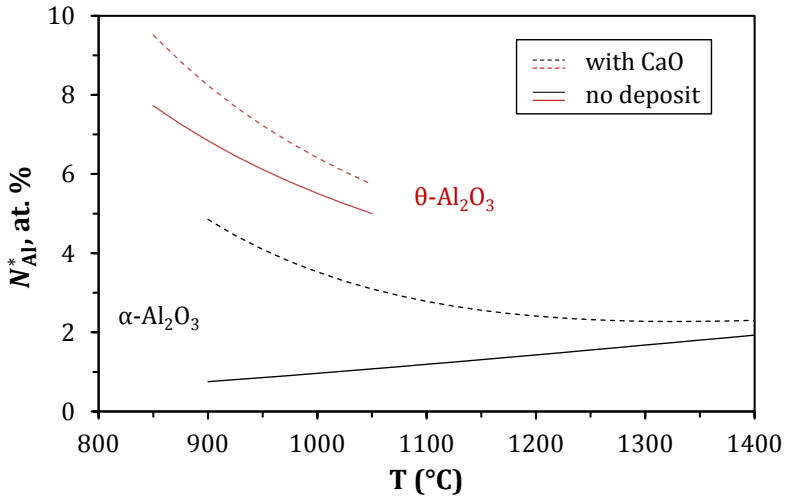

Figure 12: Minimum bulk Al content to maintain external Al_2O_3 growth with and without CaO reaction as a function of temperature. Calculated from Eqs. (25, 29), and parameters described in text.

49, 50] have shown that a temperature decrease from 1100 to 900 °C considerably delayed the $\theta \rightarrow \alpha$ transition. The value of N^*_{Al} calculated for θ-Al_2O_3 reaction with CaO at 900 °C, 8.1 at. %, is significantly higher than that obtained for α-Al_2O_3.

Uncertainties in the activation energies and the limiting assumptions used here are such that predicted N^*_{Al} values should be regarded as rough estimates. Nevertheless, the trends are valid and indicate that reaction with CaO will be significantly more severe in terms of Al consumption, relative to its availability at the metal/oxide interface, at 900 °C than at 1100 °C. This is mainly due to the persistence of θ-Al_2O_3 at the lower temperature. These observations are consistent with the observed failure of Ni–30Co–27Cr–12Al–0.1Y to passivate in the presence of CaO at 900 °C.

The above analysis neglects the multi-phase nature of the alloys studied here. Compositional changes in oxidizing multi-phase alloys have been studied in the past [51–53]. Applying a diffusional analysis to β–γ alloys shows that for a given bulk composition, the interfacial aluminum flux in steady-state conditions is greater when γ contains more Al and the volume fraction of β is correspondingly smaller. This is particularly evident using the analytical method of Ref. [51], as the minimum bulk concentration to maintain Al_2O_3 scaling according to Wagner's criterion, i.e., N^*_{Al} in Eq. (22), is to be replaced by the expression $\sqrt{N^{\gamma}_{Al}\left[N^{\gamma}_{Al} + 2f_{\beta}\left(N^{\beta}_{Al} - N^{\gamma}_{Al}\right)\right]}$, where N^i_{Al} is the Al mole fraction in phase i and f_β is the volume fraction of β. In the case of the Ni–30Co–27Cr–12Al–0.1Y alloy, as the temperature decreases, f_β increases, which is compensated by a decrease in N^{γ}_{Al}, from 9.7 at. % at 1100 °C to 7.3 at. % at 900 °C (measured by SEM–EDS). This results in a reduced interfacial Al flux, and further weighs against the alloy ability to sustain Al_2O_3 growth at the lower temperature.

5 Conclusions

Two-phase β–γ MCrAlY alloys exposed to CaO at 1100 °C were found to suffer significantly more degradation than in the absence of a deposit. The reaction with CaO proceeded according to two distinct mechanisms. During the initial stage, formation of a liquid calcium chromate led to the rapid consumption of the Cr-rich γ–phase. The extent of degradation was particularly important for a single-phase γ composition, and was significantly reduced by increasing the alloy β fraction. In a subsequent stage, a continuous Al_2O_3 layer established at the base of the scale, which led to a much lower oxidation rate. However, the protective oxide reacted with CaO to form calcium aluminates, and as its thickness was reduced, the instantaneous oxidation rate was higher than in the absence of a deposit.

Analysis of the reaction kinetics of this steady-state regime, where Al_2O_3 is simultaneously produced by oxidation of the alloy and destructed by solid-state reaction with CaO, allowed growth rates obtained by thickness-measurement and gravimetric methods to be compared. The agreement was generally good, although some discrepancy existed, which was discussed in terms of possible changes to Al_2O_3 growth mechanism due to the reaction with CaO. The analysis also led to evaluate the effect of CaO reaction on the flux of aluminum required to sustain external Al_2O_3 growth. The temperature evolution of aluminum consumption was studied by considering the activation energies for Al diffusion in the alloy, and Al_2O_3 and calcium aluminate growth. A temperature decrease to 900 °C was found to be detrimental to the kinetic stability of the protective oxide, mainly due to the longer persistence of the metastable and faster growing θ-Al_2O_3. Failure to maintain an external Al_2O_3 scale resulted for an Al-lean alloy in internal oxidation of Al, and formation of a Cr-rich oxide scale. This did not have as severe consequences as at 1100 °C since 900 °C is below the calcium chromate eutectic.

Acknowledgements

This work was supported by the Department of Energy through the University Turbine Systems Research (UTSR) Program run by the National Energy Technology Laboratory, Award Number DE-FE0007271, Seth Lawson, Project Manager. The authors thank Wei Zhao and Juan Manuel Alvarado Orozco for useful discussions on some aspects of this work.

References

[1] G. Goward, Progress in coatings for gas turbine airfoils, Surface and Coatings Technology 108-109 (1998) pp. 73–79. doi: 10.1016/S0257-8972(98)00667-7.

[2] J. R. Nicholls, Designing oxidation-resistant coatings, JOM 52 (2000) pp. 28–35. doi: 10.1007/s11837-000-0112-2.

[3] A. G. Evans, D. R. Mumm, J. W. Hutchinson, G. H. Meier and F. S. Pettit, Mechanisms controlling the durability of thermal barrier coatings, Progress in Materials Science 46 (2001) pp. 505–553. doi: 10.1016/S0079-6425(00)00020-7.

[4] B. Gleeson, Thermal barrier coatings for aeroengine applications, Journal of Propulsion and Power 22 (2006) pp. 375–383. doi: 10.2514/1.20734.

[5] A. G. Evans, D. R. Clarke and C. G. Levi, The influence of oxides on the performance of advanced gas turbines, Journal of the European Ceramic Society 28 (2008) pp. 1405–1419. doi: 10.1016/j.jeurceramsoc.2007.12.023.

[6] D. R. Clarke, M. Oechsner and N. P. Padture, Thermal-barrier coatings for more efficient gas-turbine engines, MRS Bulletin 37 (2012) pp. 891–902. doi: 10.1557/mrs.2012.232.

[7] R. Darolia, Thermal barrier coatings technology: critical review, progress update, remaining challenges and prospects, International Materials Reviews 58 (2013) pp. 315–348. doi: 10.1179/1743280413y.0000000019.

[8] J. L. Smialek, F. A. Archer and R. G. Garlick, Turbine airfoil degradation in the persian gulf war, JOM 46 (1994) pp. 39–41. doi: 10.1007/BF03222663.

[9] M. P. Borom, C. A. Johnson and L. A. Peluso, Role of environmental deposits and operating surface temperature in spallation of air plasma sprayed thermal barrier coatings, Surface and Coatings Technology 86 (1996) pp. 116–126. doi: 10.1016/s0257-8972(96)02994-5.

[10] C. Mercer, S. Faulhaber, A. Evans and R. Darolia, A delamination mechanism for thermal barrier coatings subject to calcium–magnesium–aluminosilicate (CMAS) infiltration, Acta Materialia 53 (2005) pp. 1029–1039. doi: 10.1016/j.actamat.2004.11.028.

[11] S. Kramer, J. Yang, C. G. Levi and C. A. Johnson, Thermochemical interaction of thermal barrier coatings with molten CaO-MgO-Al_2O_3-SiO_2 (CMAS) deposits, Journal of the American Ceramic Society 89 (2006) pp. 3167–3175. doi: 10.1111/j.1551-2916.2006.01209.x.

[12] C. G. Levi, J. W. Hutchinson, M.-H. Vidal-Setif and C. A. Johnson, Environmental degradation of thermal-barrier coatings by molten deposits, MRS Bulletin 37 (2012) pp. 932–941. doi: 10.1557/mrs.2012.230.

[13] Clean Coal Technology Topical Report Number 24, NETL (US Department of Energy, August 2006).

[14] V. Nagarajan, R. D. Smith and I. G. Wright, Influence of solid-state CaS-CaO-$CaSO_4$ deposits on corrosion of high-temperature alloys in simulated FBC environments, Oxidation of Metals 31 (1989) pp. 325–340. doi: 10.1007/BF00846692.

[15] K.-Y. Jung, F. S. Pettit and G. H. Meier, The effect of Ca-rich deposits on the high temperature degradation of coated and uncoated superalloys, Materials Science Forum 595–598 (2008) pp. 805–812. doi: 10.4028/www.scientific.net/MSF.595-598.805.

[16] K. T. Chiang, G. H. Meier and R. A. Perkins, The effects of deposits of CaO, $CaSO_4$, and MgO on the oxidation of several Cr_2O_3-forming and Al_2O_3-forming alloys, Journal of Materials for Energy Systems 6 (1984) pp. 71–86. doi: 10.1007/BF02833417.

[17] W. Braue, Environmental stability of the YSZ layer and the YSZ/TGO interface of an in-service EB-PVD coated high-pressure turbine blade, Journal of Materials Science 44 (2009) pp. 1664–1675. doi: 10.1007/s10853-008-3215-8.

[18] W. Braue and P. Mechnich, Recession of an EB-PVD YSZ coated turbine blade by $CaSO_4$ and Fe, Ti-rich CMAS-type deposits, Journal of the American Ceramic Society 94 (2011) pp. 4483–4489. doi: 10.1111/j.1551-2916.2011.04747.x.

[19] I. Wright and T. Gibbons, Recent developments in gas turbine materials and technology and their implications for syngas firing, International Journal of Hydrogen Energy 32 (2007) pp. 3610–3621. doi: 10.1016/j.ijhydene.2006.08.049.

[20] S. Sridhar, P. Rozzelle, B. Morreale and D. Alman, Materials challenges for advanced combustion and gasification fossil energy systems, Metallurgical and Materials Transactions A 42 (2011) pp. 871–877. doi: 10.1007/s11661-011-0627-x.

[21] B. A. Pint, High-temperature corrosion in fossil fuel power generation: Present and future, JOM 65 (2013) pp. 1024–1032. doi: 10.1007/s11837-013-0642-z.

[22] M. H. Sahraei, D. McCalden, R. Hughes and L. Ricardez-Sandoval, A survey on current advanced IGCC power plant technologies, sensors and control systems, Fuel 137 (2014) pp. 245–259. doi: 10.1016/j.fuel.2014.07.086.

[23] Materials Preparation Center, Ames Laboratory, US DOE Basic Energy Sciences, Ames, IA, USA, available from: www.ameslab.gov/mpc.

[24] C. A. Schneider, W. S. Rasband and K. W. Eliceiri, NIH image to ImageJ: 25 years of image analysis, Nature Methods 9 (2012) pp. 671–675. doi: 10.1038/nmeth.2089.

[25] V. K. Tolpygo and D. R. Clarke, Microstructural study of the theta-alpha transformation in alumina scales formed on nickel-aluminides, Materials at High Temperatures 17 (2000) pp. 59–70. doi: 10.1179/mht.2000.011.

[26] E. Levin, C. Robbins and H. McMurdie, *Phase diagrams for ceramists* vol. 1. The American Ceramic Society, Columbus, OH (1964).

[27] A. Kaiser, B. Sommer and E. Woermann, The system CaO–$CaCr_2O_4$–$CaAl_2O_4$ in air and under mildly reducing conditions, Journal of the American Ceramic Society 75 (1992) pp. 1463–1471. doi: 10.1111/j.1151-2916.1992.tb04211.x.

[28] D. Monceau and B. Pieraggi, Determination of parabolic rate constants from a local analysis of mass-gain curves, Oxidation of Metals 50 (1998) pp. 477–493. doi: 10.1023/a:1018860909826.

[29] H. Hindam and D. P. Whittle, Microstructure, adhesion and growth kinetics of protective scales on metals and alloys, Oxidation of Metals 18 (1982) pp. 245–284. doi: 10.1007/BF00656571.

[30] G. C. Rybicki and J. L. Smialek, Effect of the θ–α-Al_2O_3 transformation on the oxidation behavior of β-NiAl+Zr, Oxidation of Metals 31 (1989) pp. 275–304. doi: 10.1007/bf00846690.

[31] M. W. Brumm and H. J. Grabke, The oxidation behavior of NiAl. 1. Phase-transformations in the alumina scale during oxidation of NiAl and NiAl–Cr alloys, Corrosion Science 33 (1992) pp. 1677–1690. doi: 10.1016/0010-938x(92)90002-k.

[32] W. Weisweiler and S. J. Ahmed, Kinetik der Festkörperreaktionen im System CaO–Al_2O_3, Zement-Kalk-Gips 33 (1980) pp. 84–89.

[33] M. A. Gülgün, O. O. Popoola and W. M. Kriven, Chemical synthesis and characterization of calcium aluminate powders, Journal of the American Ceramic Society 77 (1994) pp. 531–539. doi: 10.1111/j.1151-2916.1994.tb07026.x.

[34] B. M. Mohamed and J. H. Sharp, Kinetics and mechanism of formation of monocalcium aluminate, $CaAl_2 2O_4$, Journal of Materials Chemistry 7 (1997) pp. 1595–1599. doi: 10.1039/A700201G.

[35] C. Ghoroi and A. K. Suresh, Solid–solid reaction kinetics: Formation of tricalcium aluminate, AIChE Journal 53 (2007) pp. 502–513. doi: 10.1002/aic.11086.

[36] C. Wagner, The evaluation of data obtained with diffusion couples of binary single-phase and multiphase systems, Acta Metallurgica 17 (1969) pp. 99–107. doi: 10.1016/0001-6160(69)90131-X.

[37] G. J. Yurek, J. P. Hirth and R. A. Rapp, The formation of two-phase layered scales on pure metals, Oxidation of Metals 8 (1974) pp. 265–281. doi: 10.1007/BF00609944.

[38] F. Gesmundo and F. Viani, The formation of multilayer scales in the parabolic oxidation of pure metals—I. relationships between the different rate constants, Corrosion Science 18 (1978) pp. 217–230. doi: 10.1016/S0010-938X(78)80019-5.

[39] F. Viani and F. Gesmundo, The relationships between the different rate constants and the diffusion properties of the oxides in the parabolic oxidation of a metal or a lower oxide to multilayer scales: application to the oxidation of iron, Corrosion Science 20 (1980) pp. 541–554. doi: 10.1016/0010-938X(80)90070-0.

[40] H. S. Hsu, The formation of multilayer scales on pure metals, Oxidation of Metals 26 (1986) pp. 315–332. doi: 10.1007/BF00659339.

[41] G. Wang, B. Gleeson and D. L. Douglass, Phenomenological treatment of multilayer growth, Oxidation of Metals 31 (1989) pp. 415–429. doi: 10.1007/BF00666465.

[42] A. H. Heuer, D. B. Hovis, J. L. Smialek and B. Gleeson, Alumina scale formation: A new perspective, Journal of the American Ceramic Society 94 (2011) pp. s146–s153. doi: 10.1111/j.1551-2916.2011.04573.x.

[43] J. Doychak, J. L. Smialek and T. E. Mitchell, Transient oxidation of single-crystal β–NiAl, Metallurgical Transactions A 20 (1989) pp. 499–518. doi: 10.1007/BF02653930.

[44] J. Jedlinski and G. Borchardt, On the oxidation mechanism of alumina formers, Oxidation of Metals 36 (1991) pp. 317–337. doi: 10.1007/BF00662968.

[45] B. Pint, J. Martin and L. Hobbs, The oxidation mechanism of θ-Al_2O_3 scales, Solid State Ionics 78 (1995) pp. 99–107. doi: 10.1016/0167-2738(95)00013-V.

[46] C. Wagner, Theoretical analysis of the diffusion processes determining the oxidation rate of alloys, Journal of the Electrochemical Society 99 (1952) pp. 369–380. doi: 10.1149/1.2779605.

[47] J. A. Nesbitt and R. W. Heckel, Interdiffusion in Ni-rich, Ni-Cr-Al alloys at 1100 °C and 1200 °C. II. Diffusion-coefficients and predicted concentration profiles, Metallurgical Transactions A-Physical Metallurgy and Materials Science 18 (1987) pp. 2075–2086. doi: 10.1007/bf02647079.

[48] C. E. Campbell, W. J. Boettinger and U. R. Kattner, Development of a diffusion mobility database for Ni-base superalloys, Acta Materialia 50 (2002) pp. 775–792. doi: 10.1016/s1359-6454(01)00383-4.

[49] A. Andoh, S. Taniguchi and T. Shibata, TEM observation of phase transformations of alumina scales formed on Al-deposited Fe-Cr-Al foils, Materials Science Forum 369–372 (2001) pp. 303–310. doi: 10.4028/www.scientific.net/MSF.369-372.303.

[50] Z. Li, *Investigation of the Minor-Element Effects on the Oxidation Behavior of γ-Ni + γ'-Ni_3Al Alloys.* PhD thesis University of Pittsburgh (2015). http://d-scholarship.pitt.edu/23418/.

[51] F. Gesmundo and B. Gleeson, Oxidation of multicomponent two-phase alloys, Oxidation of Metals 44 (1995) pp. 211–237. doi: 10.1007/BF01046728.

[52] P. Carter, B. Gleeson and D. Young, Calculation of precipitate dissolution zone kinetics in oxidising binary two-phase alloys, Acta Materialia 44 (1996) pp. 4033–4038. doi: 10.1016/S1359-6454(96)00054-7.

[53] T. J. Nijdam and W. G. Sloof, Modelling of composition and phase changes in multiphase alloys due to growth of an oxide layer, Acta Materialia 56 (2008) pp. 4972–4983. doi: 10.1016/j.actamat.2008.06.010.